REPORT DOCUMENTATION PAGE

Form Approved OMB NO. 0704-0188

1. REPORT DATE (DD-MM-YYYY)	2. REPORT TYPE	3. DATES COVERED (From - To)
	New Reprint	-

4. TITLE AND SUBTITLE

Large-Eddy Simulation of Shallow Water Langmuir Turbulence Using Isogeometric Analysis and the Residual-Based Variational Multiscale Method

5a. CONTRACT NUMBER

W911NF-11-1-0083

5b. GRANT NUMBER

5c. PROGRAM ELEMENT NUMBER

611102

6. AUTHORS

Andre?s E. Tejada-Marti?nez, Ido Akkerman, Yuri Bazilevs

5d. PROJECT NUMBER

5e. TASK NUMBER

5f. WORK UNIT NUMBER

7. PERFORMING ORGANIZATION NAMES AND ADDRESSES

University of California - San Diego
Office of C & G Administration
The Regents of the Univ. of Calif., U.C. San Diego
La Jolla, CA 92093 -0934

8. PERFORMING ORGANIZATION REPORT NUMBER

9. SPONSORING/MONITORING AGENCY NAME(S) AND ADDRESS(ES)

U.S. Army Research Office
P.O. Box 12211
Research Triangle Park, NC 27709-2211

10. SPONSOR/MONITOR'S ACRONYM(S)

ARO

11. SPONSOR/MONITOR'S REPORT NUMBER(S)

57917-MA.5

12. DISTRIBUTION AVAILIBILITY STATEMENT

Approved for public release; distribution is unlimited.

13. SUPPLEMENTARY NOTES

The views, opinions and/or findings contained in this report are those of the author(s) and should not contrued as an official Department of the Army position, policy or decision, unless so designated by other documentation.

14. ABSTRACT

We develop a residual-based variational multiscale (RBVMS) method based on isogeometric analysis for large-eddy simulation (LES) of wind-driven shear flow with Langmuir circulation (LC). Isogeometric analysis refers to our use of NURBS (Non-Uniform Rational B-splines) basis functions which have been proven to be highly accurate in LES of turbulent flows (Bazilevs, Y., et al. 2007, Comput. Methods Appl. Mech. Eng., 197, pp. 173–201). LC consists of stream-wise vortices in the direction of the wind acting as a secondary flow structure to

15. SUBJECT TERMS

eddy currents, flow simulation, Navier-Stokes equations, seawater, shear turbulence, turbulence, vortices

16. SECURITY CLASSIFICATION OF:			17. LIMITATION OF ABSTRACT	15. NUMBER OF PAGES	19a. NAME OF RESPONSIBLE PERSON
a. REPORT	b. ABSTRACT	c. THIS PAGE			Yuri Bazilevs
UU	UU	UU	UU		19b. TELEPHONE NUMBER: 858-534-3663

Report Title

Large-Eddy Simulation of Shallow Water Langmuir Turbulence Using Isogeometric Analysis and the Residual-Based Variational Multiscale Method

ABSTRACT

We develop a residual-based variational multiscale (RBVMS) method based on isogeometric analysis for large-eddy simulation (LES) of wind-driven shear flow with Langmuir circulation (LC). Isogeometric analysis refers to our use of NURBS (Non-Uniform Rational B-splines) basis functions which have been proven to be highly accurate in LES of turbulent flows (Bazilevs, Y., et al. 2007, Comput. Methods Appl. Mech. Eng., 197, pp. 173–201). LC consists of stream-wise vortices in the direction of the wind acting as a secondary flow structure to the primary, mean component of the flow driven by the wind. LC results from surface wave-current interaction and often occurs within the upper ocean mixed layer over deep water and in coastal shelf regions under wind speeds greater than 3 m s?1. Our LES of wind-driven shallow water flow with LC is representative of a coastal shelf flow where LC extends to the bottom and interacts with the sea bed boundary layer. The governing LES equations are the Craik-Leivobich equations (Tejada-Martínez, A. E., and Grosch, C. E., 2007, J. Fluid Mech., 576, pp. 63–108; Gargett, A. E., 2004, Science, 306, pp. 1925–1928), consisting of the time-filtered Navier-Stokes equations. These equations possess the same structure as the Navier-Stokes equations with an extra vortex force term accounting for wave-current interaction giving rise to LC. The RBVMS method with quadratic NURBS is shown to possess good convergence characteristics in wind-driven flow with LC. Furthermore, the method yields LC structures in good agreement with those computed with the spectral method in (Thorpe, S. A., 2004, Annu. Rev. Fluids Mech., 36, pp. 584 55–79) and measured during field observations in (D'Alessio, S. J., et al., 1998, J. Phys. Oceanogr., 28, pp. 1624–1641; Kantha, L., and Clayson, C. A., 2004, Ocean Modelling, 6, pp. 101–124).

REPORT DOCUMENTATION PAGE (SF298)
(Continuation Sheet)

Continuation for Block 13

ARO Report Number 57917.5-MA
Large-Eddy Simulation of Shallow Water Langm ...

Block 13: Supplementary Note

Approved for public release; distribution is unlimited.

Large-Eddy Simulation of Shallow Water Langmuir Turbulence Using Isogeometric Analysis and the Residual-Based Variational Multiscale Method

Andrés E. Tejada-Martínez
Civil & Environmental Engineering,
University of South Florida,
Tampa, FL 33620,
e-mail: aetejada@usf.edu

Ido Akkerman
Coastal & Hydraulics Laboratory,
US Army Engineer Research and
Development Center,
Vicksburg, MS 39180-6133;
Department of Structural Engineering,
University of California, San Diego,
La Jolla, CA 92093,
e-mail: iakkerman@ucsd.edu

Yuri Bazilevs
Department of Structural Engineering,
University of California, San Diego,
La Jolla, CA 92093,
e-mail: jbazilevs@ucsd.edu

*We develop a residual-based variational multiscale (RBVMS) method based on isogeometric analysis for large-eddy simulation (LES) of wind-driven shear flow with Langmuir circulation (LC). Isogeometric analysis refers to our use of NURBS (Non-Uniform Rational B-splines) basis functions which have been proven to be highly accurate in LES of turbulent flows (Bazilevs, Y., et al. 2007, Comput. Methods Appl. Mech. Eng., **197**, pp. 173–201). LC consists of stream-wise vortices in the direction of the wind acting as a secondary flow structure to the primary, mean component of the flow driven by the wind. LC results from surface wave-current interaction and often occurs within the upper ocean mixed layer over deep water and in coastal shelf regions under wind speeds greater than 3 m s^{-1}. Our LES of wind-driven shallow water flow with LC is representative of a coastal shelf flow where LC extends to the bottom and interacts with the sea bed boundary layer. The governing LES equations are the Craik-Leivobich equations (Tejada-Martínez, A. E., and Grosch, C. E., 2007, J. Fluid Mech., **576**, pp. 63–108; Gargett, A. E., 2004, Science, **306**, pp. 1925–1928), consisting of the time-filtered Navier-Stokes equations. These equations possess the same structure as the Navier-Stokes equations with an extra vortex force term accounting for wave-current interaction giving rise to LC. The RBVMS method with quadratic NURBS is shown to possess good convergence characteristics in wind-driven flow with LC. Furthermore, the method yields LC structures in good agreement with those computed with the spectral method in (Thorpe, S. A., 2004, Annu. Rev. Fluids Mech., **36**, pp. 584 55–79) and measured during field observations in (D'Alessio, S. J., et al., 1998, J. Phys. Oceanogr., **28**, pp. 1624–1641; Kantha, L., and Clayson, C. A., 2004, Ocean Modelling, **6**, pp. 101–124).* [DOI: 10.1115/1.4005059]

1 Introduction

Wave effects play an important role in determining surface boundary fluxes of momentum, energy and scalars and ultimately vertical mixing [1]. Wave-current interaction is among several flow phenomena generating turbulence in the ocean; others include wind-and tidal-driven shear, buoyancy-driven convection and wave breaking. Wind speeds greater than 3 m s^{-1} often lead to wave-current interaction sufficiently strong to generate Langmuir circulation (LC), consisting of pairs of parallel counter-rotating vortices (or cells) oriented approximately in the downwind direction, as shown in the sketch in Fig. 1. The cells are characteristic of the turbulence (i.e., the Langmuir turbulence) advected by the mean flow.

The surface convergence of each cell generates a downwelling region characterized by negative vertical velocity fluctuations while the bottom divergence generates an upwelling region characterized by positive vertical velocity fluctuations, leading to increased levels of mixing. Bubbles, particulate matter and flotsam accumulate along the surface convergence of the cells forming what are often referred to as "windrows." Surface convergences of the cells are characterized by intensification of positive downwind velocity fluctuations leading to an enhanced mean current as seen in Fig. 1.

Historically, Langmuir cells have been measured within the upper ocean surface mixed layer in deep water far above the bottom (Fig. 1). However, Gargett et al. (2004) reported detailed acoustic Doppler current profiler (ADCP) measurements of Langmuir cells engulfing the entire water column lasting as long as 18 hs in a shallow water region off the coast of New Jersey. Measurements were made at Rutgers' LEO15 cabled observatory in 15 m depth water. Gargett et al. (2004) denoted the observed full-depth cells as Langmuir supercells (LSC) because of their important contribution towards transport of sediment and bioactive material on shallow shelves. The strong coherence of LSC makes them more effective than classical bottom boundary layer turbulence at moving material out of the low-speed layer near bottom and into the strong and strongly directional downwind mean flow associated with these events. Gargett et al. (2004) suggested that transport in such supercell events dominates net annual transport of sediment at LEO15.

Originally described by Langmuir [2], LC is now generally accepted to be the result of wave-current interaction or, more specifically, the interaction between the wind-driven shear current and the Stokes drift current induced by surface gravity waves [2]. As with all turbulence, Langmuir turbulence encompasses a range of spatial and temporal scales. Among the larger spatial scales are those of the cells which extend in the downwind direction for tens of meters to kilometers and are separated by distances ranging from meters to as much as a kilometer [3].

A mechanism for the generation of LC was first proposed by Craik and Leibovich [4]. It consists of a vortex force (the Craik-Leibovich force or C-L force) in the momentum equations representing the interaction between the Stokes drift velocity, induced by surface gravity waves, and the vertical shear of the current; specifically, the C-L vortex force is the vector cross product between the Stokes drift velocity and the vorticity of the flow. Main parameter ingredients in this force are the dominant wavelength and amplitude of the surface waves used to define the Stokes drift velocity profile. The square root of the ratio of wind friction velocity to surface Stokes drift velocity defines the

Contributed by the Applied Mechanics Division of ASME for publication in the Journal of Applied Mechanics. Manuscript received March 12, 2011; final manuscript received April 20, 2011; published online December 13, 2011. Assoc. Editor: Tayfun E. Tezduyar.

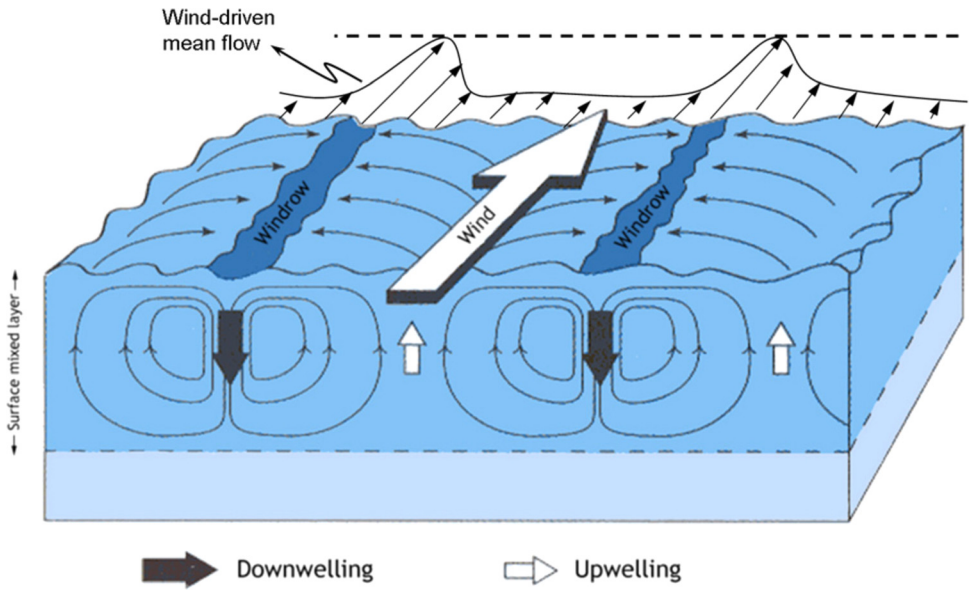

Fig. 1 Sketch of Langmuir circulation spanning the upper ocean mixed layer

turbulent Langmuir number, La_t, a measure of the strength of wind-driven shear forcing relative wave forcing [5]. The strength of the Langmuir cells is thus inversely proportional to La_t. Although this definition is counterintuitive, it is widely used within the LES community [6]. A more intuitive definition is described in Ref. [7] as the ratio of Stokes production of turbulence kinetic energy (TKE) to shear production of TKE. In this definition, the strength of the Langmuir turbulence increases with La_t.

The C-L force arises from low-pass time filtering or wave-phase averaging of the Navier-Stokes equations in order to filter out the high frequency surface waves. Hereafter, the time filtered Navier-Stokes equations with the C-L force will be referred to as the C-L equations. Inclusion of the C-L force in the momentum equation greatly reduces the computational complexity as it eliminates the need to resolve the surface waves giving rise to LC. Instead, the top of the flow domain is simply taken to be bounded by a flat (nondeforming) surface denoting the mean water height. Note that the C-L framework does not account for the impact of wave-breaking on the turbulence resolved. Sullivan and McWilliams [8] have incorporated a stochastic model of wave breaking to the C-L equations in their LES of Langmuir circulations within the upper ocean mixed layer.

The C-L equations have enabled a number of successful LES (large-eddy simulations) and RANS (simulations based on the Reynolds averaged Navier-Stokes equation) describing the vertical and horizontal structure of upper ocean Langmuir turbulence in statistical equilibrium, e.g., [5,9,10–13]. See the review in Ref. [10] for further references. In direct numerical simulation (DNS) all of the scales of a turbulent flow are explicitly computed while in RANS, only the mean component of the flow is explicitly computed and the turbulent scales or eddies are parameterized. Large-eddy simulations is a compromise between the computationally expensive DNS and the less demanding RANS. In LES the more energetic, larger eddies are explicitly computed while the smaller eddies are modeled [14]. Note that a DNS of Langmuir turbulence would not be possible with the C-L equations, as these equations are the result of time filtering. A DNS would require a prohibitedly expensive simulation resolving surface waves and thus direct resolution of the interaction between surface waves and the shear current giving rise to Langmuir circulation.

Of particular interest here is the work of Tejada-Martínez and Grosch [9] who performed LES of a finite-depth, wind-driven shear current with full-depth Langmuir circulation guided by the measurements in Refs. [15,16]. Their LES used the C-L equations. In particular, predictions from the LES compared favorably with in-water measurements of the Reynolds stress components. Furthermore, the structure of the Langmuir cells, manifested as a secondary turbulent structure in the shear flow, was consistent with that measured during the in-water observations.

Ideally, computational methods for turbulent flow must be able to resolve, or accurately model all the relevant flow scales and their interactions in the presence of complex geometrical configurations. Currently, computational approaches for turbulent flows include efficient techniques that are based on high-order functions (e.g., global polynomial and Fourier bases) able to accurately represent the small scale physics in turbulent processes at relatively high Reynolds numbers, albeit on very simple geometrical configurations. For example, LES performed with the C-L equations have focused on simple flow configurations while accurately resolving complex physical phenomena such as upper ocean mixed layer (UOML) turbulence and internal waves in the pycnocline below the UOML [17,18]. On the other end of the spectrum, much progress has been made over the last several decades on the computation of flows over complex geometrical configurations. These methods, based on low-order functional representations, are able to represent relatively well the gross features of a given turbulent flow, yet they do not possess the high-order accuracy of the aforementioned spectral techniques to predict the more detailed features of the flow. Thus, it appears that there is a gap between techniques capable of accurately resolving all scales in turbulent flows on simple geometries and techniques capable of resolving only large scale (gross) features on complex geometries. In order to bridge this gap, a methodology is necessary that simultaneously possesses superior approximation and uniform convergence behavior over a wide range of spatial and temporal scales, necessary for capturing flow physics, and the geometrical flexibility, necessary for geophysical and engineering applications. We feel that isogeometric analysis based on Non-Uniform Rational B-splines (NURBS), recently proposed as a new computational technique by Hughes et al. [19], is an excellent candidate for the task. NURBS are spline basis functions used for representation of complex geometry, are locally supported, and possess spectrallike approximation properties compared to standard complex-geometry approaches (i.e., low-order finite elements and finite volumes).

In this paper, we extend variational multiscale turbulence modeling procedures to the C-L equations and implement them using isogeometric analysis based on NURBS. In the case of the Navier-Stokes equations, this framework has been shown to yield spectral-like resolution while rapidly converging under refinement to direct numerical simulation (DNS), and providing good quality large-eddy simulation (LES) results on intermediate meshes (e.g., see Bazilevs

et al. [20]), for both homogeneous as well as boundary layer and transitional flows. Extension of these methodologies to the C-L equations will allow future research investigating effects of complex lateral boundaries and bathymetry on Langmuir circulation and other salt and momentum mixing processes in coastal oceans and estuaries.

Solution of the Navier-Stokes equation augmented with the C-L vortex force is nontrivial as the latter term is an advective term giving rise to instabilities requiring stabilization of the type presented in this paper. Note that the C-L vortex force has been previously identified in Refs. [10] and [21] as giving rise to instabilities by triggering scales of size smaller than the grid (i.e., subgrid-scales). The goal of this paper is the nontrivial extension of advection stabilization within a variational formulation in order to consistently account for the advective nature of the C-L vortex force. Advection stabilization behaves as a subgrid-scale model derived from the Navier-Stokes equations (in our case the Navier-Stokes equations augmented with the C-L vortex force) via a splitting of the space of solutions. The splitting results in finite-dimensional equations governing the large-eddies and infinite dimensional equations governing unresolved eddies. Analytical expressions for the solution of the latter are obtained via mathematical approximations [1]. The splitting of the space of solutions does not involve application of spatial filtering nor does it generate a residual subgrid-scale stress, as is the case in classical LES. In this approach the subgrid-scale model is not for the subgrid-scale stress, but rather for a subgrid-scale velocity. Thus, a conventional subgrid-scale stress is not present in the formulation. As noted earlier, Bazilevs et al. [20] have shown that this approach yields LES solutions on intermediate meshes while rapidly converging to direct numerical simulation (DNS) solutions on finer meshes. Their simulations involved turbulent channel flows and forced isotropic turbulence.

2 Numerical Approach

In the following subsections we provide precise details of the numerical method deployed for solving the Craik-Leibovich equations.

2.1 The Craik-Leibovich Equations at the Continuous Level. Let $\Omega \in \mathbb{R}^3$ be the problem domain and let $\partial\Omega$ denote its boundary. A conservative form of the dimensionless Navier-Stokes equations, with C-L forcing, in the Eulerian frame are taken as a starting point of our developments, and are given as

$$\frac{\partial \boldsymbol{u}}{\partial t} + \nabla \cdot (\boldsymbol{u} \otimes \boldsymbol{u}) + \nabla p - \nabla \cdot (2Re^{-1}\nabla^s \boldsymbol{u}) - La_t^{-2}\phi \times \nabla \times \boldsymbol{u} = 0 \text{ in } \Omega \tag{1}$$

$$\nabla \cdot \boldsymbol{u} = 0 \text{ in } \Omega \tag{2}$$

Equations (1) and (2) represent conservation of linear momentum and mass, respectively, assuming density is constant. In the above $\boldsymbol{u}$ and p are the fluid velocity and pressure (divided by density), $\nabla^s = (1/2)(\nabla + (\nabla)^T)$ is the symmetric spatial gradient of the velocity, $\boldsymbol{\phi}$ is the Stokes drift velocity and $\mathbf{f}$ is the body force per unit mass. The physical nature of the flow is characterized by the dimensionless Reynolds and turbulent Langmuir numbers, Re and La_t, respectively. The turbulent Langmuir number is inversely proportional to the strength of Langmuir circulation (i.e., wave forcing) relative to the shear flow (i.e., wind forcing) in the model.

The last term on the left-hand-side of Eq. (1) represents C-L forcing. Because the term depends on the first-order derivatives of the velocity field, it has the mathematical structure of advection. With this in mind, we re-write the C-L momentum equations as

$$\frac{\partial \boldsymbol{u}}{\partial t} + \nabla \cdot (\boldsymbol{u} \otimes \boldsymbol{u}) + \nabla p - \nabla \cdot (2Re^{-1}\nabla^s \boldsymbol{u}) + \tilde{\mathbf{A}}_i \frac{\partial \boldsymbol{u}}{\partial x_i} = \mathbf{f} \text{ in } \Omega \tag{3}$$

where $\tilde{\mathbf{A}}_i$'s are

$$\tilde{\mathbf{A}}_1 = La_t^{-2}\begin{pmatrix} 0 & -\phi_2 & \phi_3 \\ 0 & \phi_1 & 0 \\ 0 & 0 & \phi_1 \end{pmatrix} \tag{4}$$

$$\tilde{\mathbf{A}}_2 = La_t^{-2}\begin{pmatrix} \phi_2 & 0 & 0 \\ -\phi_1 & 0 & -\phi_3 \\ 0 & 0 & \phi_2 \end{pmatrix} \tag{5}$$

$$\tilde{\mathbf{A}}_3 = La_t^{-2}\begin{pmatrix} \phi_3 & 0 & 0 \\ 0 & \phi_3 & 0 \\ -\phi_1 & -\phi_2 & 0 \end{pmatrix} \tag{6}$$

and summation on the repeated index i is employed. In the following section we present the numerical formulation of the above partial differential equations.

2.2 The Space-Discrete Formulation of the Craik-Leibovich Equations. In this section we present the residual-based variational multiscale (RBVMS) formulation of the C-L partial differential equations. The formulation is a straight-forward extension of the RBVMS formulation for the incompressible Navier-Stokes equations [20,22] that also accounts for the presence of the C-L forcing terms. For better approximation of thin boundary layers near no-slip walls, weak enforcement of the Dirichlet boundary conditions, proposed in Ref. [23], is also employed.

Let $\mathcal{V}^h$ denote the discrete solution space for the velocity-pressure pair $\{\boldsymbol{u}^h, p^h\}$ and let $\mathcal{W}^h$ denote the discrete weighting space for the linear momentum and continuity weighting functions $\{\delta\boldsymbol{u}^h, \delta p^h\}$.

The space-discrete Navier-Stokes problem is stated as: Find $\{\boldsymbol{u}^h, p^h\} \in \mathcal{V}^h$ such that $\forall \{\delta\boldsymbol{u}^h, \delta\mathbf{p}^h\} \in \mathcal{W}^h$,

$$B(\{\delta\boldsymbol{u}^h, \delta p^h\}, \{\boldsymbol{u}^h, p^h\}) + B_{vms}(\{\delta\boldsymbol{u}^h, \delta p^h\}, \{\boldsymbol{u}^h, p^h\}) + B_{wbc}(\{\delta\boldsymbol{u}^h, \delta p^h\}, \{\boldsymbol{u}^h, p^h\}) = (\delta\boldsymbol{u}^h, \mathbf{f})_\Omega + (\delta\boldsymbol{w}, \mathbf{h})_{\Gamma_h} \tag{7}$$

In the above, $(\cdot,\cdot)_A$ denotes an L_2-inner product over A and Γ_h is a part of the domain boundary where traction $\mathbf{h}$ is applied. In this work, the last term on the right-hand-side of Eq. (7) is active and models the effect of wind stress on the water surface. The rest of the terms of the above formulation are defined in what follows.

$$B(\{\boldsymbol{w}, q\}, \{\boldsymbol{u}, p\}) = \left(\boldsymbol{w}, \frac{\partial \boldsymbol{u}}{\partial t}\right)_\Omega - (\nabla \boldsymbol{w}, \boldsymbol{u} \otimes \boldsymbol{u})_\Omega + (q, \nabla \cdot \boldsymbol{u})_\Omega - (\nabla \cdot \boldsymbol{w}, p)_\Omega + \left(\boldsymbol{w}, \tilde{\mathbf{A}}_i \frac{\partial \boldsymbol{u}}{\partial xi}\right)_\Omega + (\nabla^s \boldsymbol{w}, 2Re^{-1}\nabla^s \boldsymbol{u})_\Omega \tag{8}$$

is the Galerkin part of the weak form

$$B_{vms}(\{\boldsymbol{w}, q\}, \{\boldsymbol{u}, p\}) = -(\nabla \boldsymbol{w}, \boldsymbol{u}' \otimes \boldsymbol{u} + \boldsymbol{u} \otimes \boldsymbol{u}' + \boldsymbol{u}' \otimes \boldsymbol{u}')_\Omega - \left(\tilde{\mathbf{A}}_i^T \frac{\partial \boldsymbol{u}}{\partial xi}, \boldsymbol{u}'\right)_\Omega - (\nabla \cdot \boldsymbol{w}, p')_\Omega - (\nabla q, \boldsymbol{u}')_\Omega. \tag{9}$$

are the RBVMS terms, and the pair $\{\boldsymbol{u}', p'\}$ denotes the velocity and pressure subgrid scales (i.e., the scales that are too small to be reasonably approximated on a given mesh).

Analogously to Ref. [20], the subgrid scales are modeled as

$$\boldsymbol{u}' = -\tau_{\mathbf{M}}\left(\frac{\partial \boldsymbol{u}}{\partial t} + \boldsymbol{u}\nabla \boldsymbol{u} + \nabla p - Re^{-1}\Delta \boldsymbol{u} + \tilde{\mathbf{A}}_i \frac{\partial \boldsymbol{u}}{\partial x_i} - \mathbf{f}\right)$$
$$p' = -\tau_C \nabla \cdot \boldsymbol{u} \tag{10}$$

where $\tau_{\mathbf{M}}$ and τ_C are the subgrid-scale parameters defined in what follows. The subgrid-scale parameters are also known as the stabilization parameters due to the similarities between RBVMS and

stabilized methods [24–26]. In fact, stabilized methods are the progenitors of the RBVMS methodology. Note that the fine scales are proportional to the residual of the C-L partial differential equations, which renders the numerical methodology consistent. Also note that the momentum equation residual is in the advective form, which may be derived from the conservative form given by Eq. (1) using the incompressibility constraint from Eq. (2).

To define the subgrid-scale parameters for the C-L equations, the momentum equations are written in the form of a quasi-linear advective-diffusive system as

$$\frac{\partial \boldsymbol{u}}{\partial t} + \mathbf{A}_i \frac{\partial \boldsymbol{u}}{\partial x_i} - Re^{-1}\Delta \boldsymbol{u} = \mathbf{f} - \nabla p \quad \text{in} \quad \Omega, \tag{11}$$

where $\mathbf{A}_i = (u_i \mathbf{I} + \tilde{\mathbf{A}}_i)$ are the advective flux jacobians given by

$$\mathbf{A}_1 = \begin{pmatrix} u & -\phi_2 & -\phi_3 \\ 0 & u+\phi_1 & 0 \\ 0 & 0 & u+\phi_1 \end{pmatrix} \tag{12}$$

$$\mathbf{A}_2 = \begin{pmatrix} v+\phi_2 & 0 & 0 \\ -\phi_1 & v & -\phi_3 \\ 0 & 0 & v+\phi_2 \end{pmatrix} \tag{13}$$

$$\mathbf{A}_3 = \begin{pmatrix} w+\phi_3 & 0 & 0 \\ 0 & w+\phi_3 & 0 \\ -\phi_1 & -\phi_2 & w \end{pmatrix}. \tag{14}$$

The C-L forcing contributions render these jacobians nondiagonal and nonsymmetric, which requires an appropriate definition of the subgrid-scale parameters. Based on the developments in Ref. [27–29] for advective-diffusive systems, they may be computed as follows:

$$\tau_{\mathbf{M}} = \left(\frac{4}{\Delta t^2}\mathbf{I} + G_{ij}\mathbf{A}_i\mathbf{A}_j + C_I G_{ij} G_{ij} Re^{-2}\mathbf{I} \right)^{-\frac{1}{2}} \tag{15}$$

where

$$G_{ij} = \frac{\partial \xi_k}{\partial x_i}\frac{\partial \xi_k}{\partial x_i} \tag{16}$$

is the metric-tensor of the mapping from the parametric to the physical domain of the NURBS element, and C_I is a constant arising in the element-level inverse estimate (see, e.g., Ref. [30]).

The definition of $\tau_{\mathbf{M}}$ in Eq. (15) necessitates the computation of the matrix square root inverse. We do so using the Denman-Beavers algorithm [31], which computes the matrix square root inverse in an iterative fashion. The algorithm is started by setting $\mathbf{X}_0 = \tau_{\mathbf{M}}{}^{-2}$ and $\mathbf{Y}_0 = \mathbf{I}$, and the iteration consists of the following updates:

$$\begin{aligned} \mathbf{X}_{k+1} &= \frac{1}{2}\left(\mathbf{X}_k + \mathbf{Y}_k^{-1}\right) \\ \mathbf{Y}_{k+1} &= \frac{1}{2}\left(\mathbf{Y}_k + \mathbf{X}_k^{-1}\right) \end{aligned} \tag{17}$$

where k is the iteration index. In a small number of iterations $\mathbf{Y}$ converges to τ_M defined by Eq. (15). Given $\tau_{\mathbf{M}}$, τ_C is computed as

$$\tau_C = (G_{ij}\tau_{Mij})^{-1} \tag{18}$$

which is a generalization of the relationship given in Refs. [20,32]

An alternative definition of the subgrid-scale parameters $\tau_{\mathbf{M}}$ and τ_C based on the element-level matrices and vectors may be employed in our discrete formulation. The subgrid-scale parameter definitions given in Ref. [33] may be naturally extended to the C-L equations, which is likely to improve the accuracy and robustness of the numerical method for small time step sizes [34]. However, we did not pursue this approach here.

Finally, B_{wbc}, defined as

$$\begin{aligned} \boldsymbol{B}_{wbc}(\{\boldsymbol{w},q\},\{\boldsymbol{u},p\}) = {} & (\boldsymbol{w}, -2Re^{-1}\nabla^s \boldsymbol{u}\cdot\mathbf{n})_{\Gamma_g} \\ & + (-2Re^{-1}\nabla^s \boldsymbol{w}\cdot\mathbf{n}, (\boldsymbol{u}-\boldsymbol{g}))_{\Gamma_g} \\ & + (\boldsymbol{w}, \tau_B(\boldsymbol{u}-\mathbf{g}))_{\Gamma_g} \end{aligned} \tag{19}$$

contains terms that weakly impose the boundary condition $\boldsymbol{u} = \mathbf{g}$. In Eq. (19), Γ_g is the Dirichlet part of the problem domain boundary and $\mathbf{g}$ is the prescribed flow velocity vector. In the formulation we assume that the normal component of the flow velocity vector is imposed strongly. To ensure numerical stability and optimal convergence, the penalty parameter τ_B in Eq. (19) is chosen as

$$\tau_B = C_b Re^{-1}\sqrt{n_i G_{ij} n_j} \tag{20}$$

where n_i's are the Cartesian component of the unit outward normal vector to Γ_g and C_b is an elementwise constant emanating from a boundary inverse estimate [23]. Further discussion and computational results employing weakly-enforced Dirichlet conditions may be found in Refs. [23,32,35,36].

3 Computational Setup

The computational domain, depicted in Fig. 2, is a rectangular box with dimensions $2\pi\delta \times 2\delta \times (8/3)\pi\delta$, in the stream-wise or downwind (x), wall-normal or vertical (y), and span-wise or cross-wind (z) directions, respectively. The half-depth of the domain (in the y-direction) is δ. The flow is driven by a wind stress in the x direction applied at the top surface ($y = 2\delta$), where no-penetration boundary condition is also assumed to hold. No-slip conditions (enforced weakly) are applied at the bottom wall boundary ($y = 0$). In the stream-wise and span-wise directions periodic boundary conditions are employed in order to represent an unbounded domain in these directions, approximating a continental shelf flow miles away from coastal boundaries.

Characteristic flow velocity, Stokes drift velocity and length are taken as wind stress friction velocity u_τ, Stokes drift velocity at the surface u_s, and half-depth δ, respectively. Characteristic time scale is taken as δ/u_τ. Using these scales to nondimensionalize the C-L equations gives rise to the Reynolds number defined as $Re = u_\tau\delta/\nu$ (where ν is kinematic viscosity) and the turbulent Langmuir number defined as

$$La_t = \sqrt{u_\tau/u_s}$$

The nondimensional Stokes drift $\boldsymbol{\phi}$ in Eq. (1) is given by

$$\boldsymbol{\phi} = \begin{pmatrix} \dfrac{\cosh(2\kappa y)}{2\sinh(2\kappa\delta)} \\ 0 \\ 0 \end{pmatrix} \quad y \in [0, 2\delta] \tag{21}$$

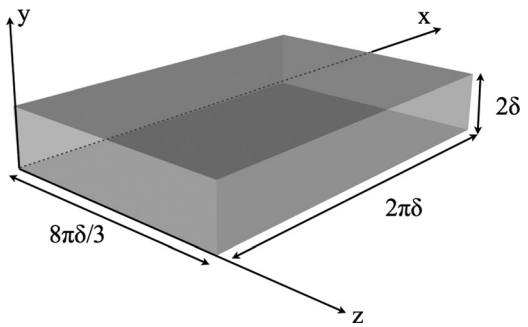

Fig. 2 Computational domain

where $\kappa = 2\pi/\gamma$ is the dominant wave number and γ is the dominant wavelength of surface gravity waves generating Langmuir circulation (see Refs. [37,38] for details). In their LES of Langmuir circulation within the upper ocean mixed layer in deep water, Harcourt and DAsaro [39] have used a Stokes drift velocity in the C-L force representative of wind seas characterized by broadband equilibrium displacement that represent the cumulative effect over some fetch or duration of surface stress due to local wind conditions. Their broadband wave spectra have Stokes drift composed of a Stokes drift spectrum with elements that decay exponentially below the surface.

The flow is driven purely by a wind stress; thus the body force, **f,** in Eq. (1) is **0**. The dimensionless wind stress, **h**, is given by

$$\mathbf{h} = \begin{pmatrix} 1 \\ 0 \\ 0 \end{pmatrix} \tag{22}$$

We note that setting $\phi = \mathbf{0}$ and keeping the same boundary conditions gives a similar flow configuration similar to traditional Couette flow, but with a surface wind-stress and a stationary no-slip bottom instead of the usual no-slip bottom and top plates moving in opposite direction to each other.

For the computations presented here, we set $Re = 395$, $La_t = 0.7$, and $\lambda = 12\delta$. These are identical to the parameters reported in spectral LES calculations of Ref. [9]. Furthermore, parameters $La_t = 0.7$ and $\lambda = 12\delta$ are characteristic of the wind and wave forcing conditions during the field measurements of shallow water, full-depth Langmuir circulation of Gargett and Wells [16]. Their measurements were made in a 15 ms-deep water column on the coastal shelf off southern New Jersey.

Quadratic NURBS that are C^1-continuous across mesh knots are employed in the computations. We perform our simulations using a sequence of h-refined meshes to ensure convergence of the computational results. The coarsest mesh is comprised of $24 \times 26 \times 24$ NURBS elements, while the finest mesh has $64 \times 66 \times 64$ NURBS elements. In general, for NURBS of order p and maximal continuity $p-1$, the number of basis functions in each tensor-product direction equals to $n+p$, where n is the number of elements in this direction. (For periodic boundary conditions, the number of basis functions is n, which is independent of the polynomial order.) This is in contrast to the C^0-continuous finite elements of order p, where the number of basis functions is $pn+1$ (or pn in the periodic case). This amounts to significant savings in the number of degrees of freedom for NURBS elements with respect to finite elements of the same order, especially in 3D.

The mesh is uniform in the periodic directions. The elements in the wall-normal (vertical) direction are stretched toward the top and bottom boundaries. The mesh knots are placed according to

$$y_i = b^{-1} \tanh\left(\left(\frac{2i}{N_y+1} - 1\right) \tanh^{-1}(b)\right) \quad i \in [1, N_y+1] \tag{23}$$

where $b = 0.973$ is used

The flow is advanced in time using the generalized-α method [40,41] and the resulting nonlinear equations are solved using an inexact Newton Krylov approach (see Ref. [20] for details). Details of the mesh and time step sizes may be found in Table 1.

4 Numerical Results

In the following sub-sections we present results from LES of wind-driven flow with and without Langmuir circulation (LC). In the description of these results, components of the velocity vector $\boldsymbol{u}$ are referred to as either (u_1, u_2, u_3) or (u, v, w) where u_1 (u), u_2 (v) and u_3 (w) are velocity components in the stream-wise (downwind), wall-normal (vertical) and span-wise (crosswind) directions, respectively.

Table 1 Summary of mesh and time step sizes used in the simulations. In the table, N_x, N_y, and N_z are the number of basis functions used in the simulation in each tensor product direction and N_{tot} is their total number. y_1^+ is the size of the first element in the wall-normal direction in non-dimensional wall units ($y_1^+ = u_\tau \Delta y/\nu$). Time step size Δt has been made dimensionless with characteristic time scale given as δ/u_τ.

N_x	N_y	N_z	N_{tot}	y_1^+	Δt
24	26	24	14976	4.62	0.025
32	34	32	34816	3.31	0.0188
48	50	48	115200	2.11	0.0125
64	66	64	270336	1.55	0.00935

4.1 Flow Structures. Figure 3 shows an instantaneous three-dimensional snapshot of iso-contours of vertical velocity fluctuations in the wind-driven flow with LC. Vertical velocity fluctuations are characterized by negative and positive downwind elongated regions, corresponding to the downwelling and upwelling limbs of the Langmuir cells sketched in Fig. 1. Figure 4 shows an instantaneous snapshot of downwind velocity fluctuations in wind-driven flows with and without LC. In both flows, downwind velocity fluctuation is characterized by downwind elongated streaks alternating in sign in the crosswind direction. The simulation with LC was initialized by "turning on" the C-L vortex force in the simulation without LC after the latter had achieved statistical equilibrium. Animations (not shown) reveal that the vortex force causes the positive streaks in the flow without LC to merge together leading to a single pair of streaks (positive and negative). The crosswind extent of the resulting positive streak is greater than the negative streak.

In order to reveal the crosswind-vertical structure of the previously described downwind elongated streaks, we perform the following triple decomposition of the computed velocity:

$$u_i = \langle u_i \rangle + \underbrace{\langle u_i' \rangle_{tx} + u_i''}_{=u_i'} \tag{24}$$

where $\langle \cdot \rangle_{tx}$ denotes averaging in time and over the downwind (x) direction and the instantaneous velocity fluctuation is obtained via the classical Reynolds decomposition:

$$u_i = \langle u_i \rangle + u_i' \tag{25}$$

where brackets without subscripts denote averaging over downwind (x) and crosswind (z) directions and over time. Note that the prime notation used here to define the resolved turbulence velocity fluctuation is different from the prime notation in Eqs. (9) and (10) used to define unresolved (subgrid) scales. The middle term on the right hand side of Eq. (24) is defined as a partially averaged fluctuation:

$$v_i'(y,z) = \langle u_i' \rangle_{tx} \tag{26}$$

This partially averaged velocity fluctuation emphasizes coherent, secondary flow structures in the downwind direction such as the downwind elongated streaks observed in Fig. 4. Figures 5 and 6 show the crosswind-vertical structure of the partially averaged velocity fluctuation in the flows with and without LC, respectively. Overall, both cases exhibit positive and negative crosswind cell structures in each of the partially averaged fluctuating velocity components; the flow with LC has a spanwise one-cell structure while the flow without LC has a less coherent spanwise two-cell structure.

The one-cell structure in the flow with C-L forcing (Fig. 5) is nearly identical to that obtained with the spectral LES of Tejada-Martínez and Grosch [9] with the same wind and wave forcing

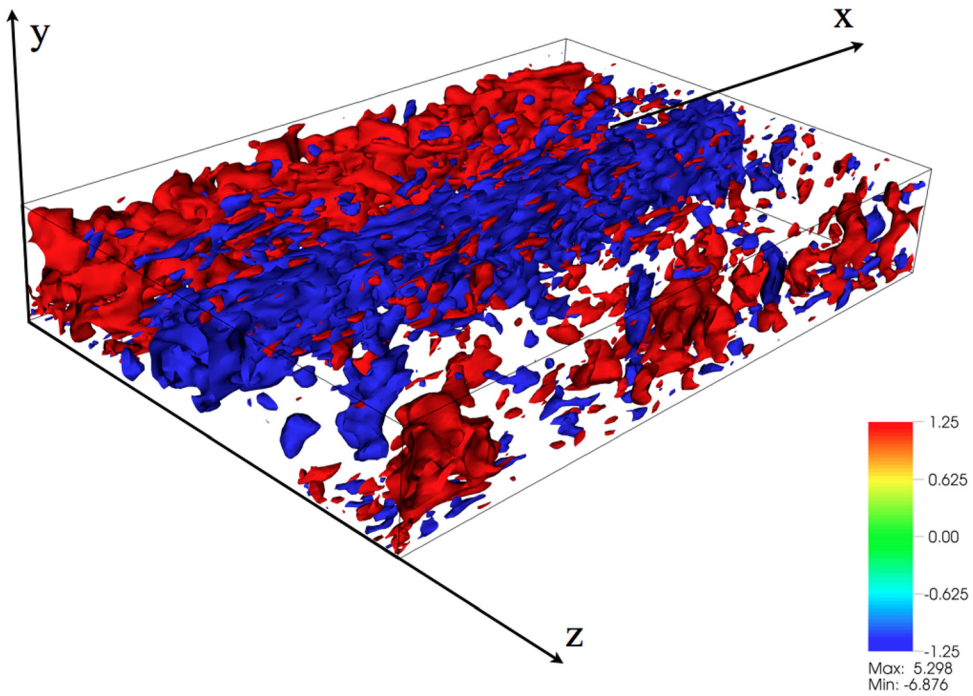

Fig. 3 Instantaneous snapshot of iso-contours of wall-normal (vertical) velocity fluctuations in flow with LC on the 64 × 66 × 64 quadratic NURBS mesh described earlier

parameters described earlier. Recall that these parameters in the C-L vortex force have been chosen as $La_t = 0.7$ and $\gamma = 12\delta$ following the field measurements of Ref. [16]. Additionally, the one-cell structure in the flow with C-L forcing possesses all of the basic characteristics of full-depth Langmuir circulation expected based on the field measurements in Ref. [16]. Experimental data in Ref. [16] shows that the spanwise (crosswind) length of one Langmuir cell is in the range of 6δ and 12δ. Accordingly, our computation has predicted the generation of only one Langmuir cell as expected, given the crosswind extent chosen for the domain (see Fig. 2).

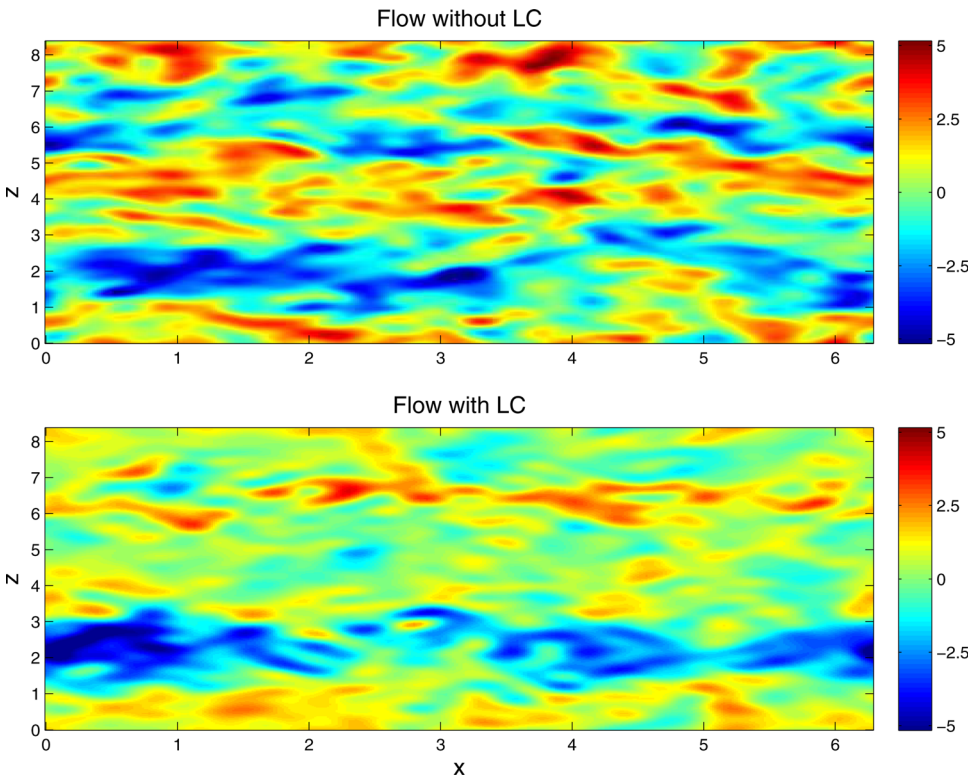

Fig. 4 Color maps of instantaneous downwind velocity fluctuation u_1 on the downwind-crosswind plane at mid-depth in flows with and without C-L vortex forcing (i.e., with and without LC). Results are from the simulations on the 48 × 50 × 48 quadratic NURBS mesh described earlier.

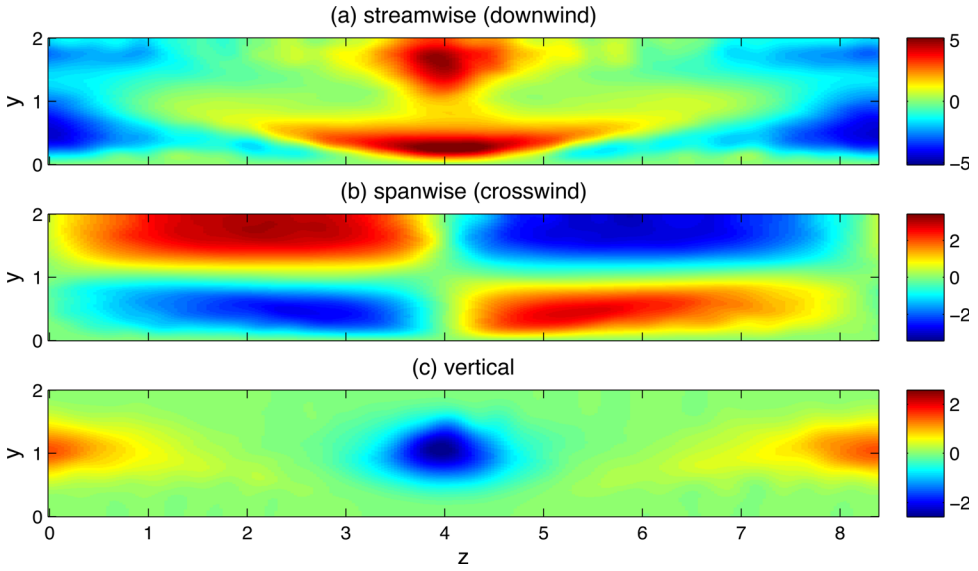

Fig. 5 Crosswind-vertical variation of velocity fluctuations v_i' (defined in Eq. (26)) in flow with LC. Results are from the simulation on the 48 × 50 × 48 quadratic NURBS mesh.

As seen in Fig. 5, a change in sign of surface intensified v_3' (in panel (*b*) generates the surface convergence of the cell, which in turns leads to the downwelling limb of the cell. The downwelling limb is the full-depth region characterized by negative v_2' (in panel (*c*)). This region is depicted in the sketch shown in Fig. 1. Furthermore, the upwelling limb (region with positive v_2') of the cell is larger in crosswind extent than the downwelling region (region with negative v_2') in agreement with the field measurement of full-depth LC in Ref. [16]. At mid depth the upwelling limb is approximately 1.6 larger than the down-welling limb, which is close to the 1.4 factor measured in the field. The downwelling limb coincides with a region of bottom-and surface-intensified positive v_1' (in panel (*a*)). Note that this region of full-depth positive v_1' leads to an enhanced downwind current as depicted in Fig. 1. The enhancement of the downwind current within the Langmuir cell downwelling region is by a factor of approximately 10 u_* near the surface and near the bottom of the water column. Finally, the one-cell structure in the flow with C-L vortex forcing (Fig. 5) is significantly different in structure and magnitude of fluctuations from the two-cell structure obtained in the flow without C-L vortex forcing (Fig. 6).

In Fig. 7, the instantaneous velocity fluctuations have been made dimensional with the wind stress friction velocity reported by Gargett and Wells in Ref. [16] during their field observations of full-depth Langmuir cells. Magnitudes of these fluctuations in our LES are in close agreement with those measured in the field (shown in Fig. 8) as well as with those computed using the spectral method of Tejada-Martínez et al. [9,21]. In both, computations and field experiments, instantaneous streamwise and spanwise velocity fluctuations are in the ±8 cm/s range and the vertical velocity fluctuation is in the ±4 cm/s range. Note that the field measurements in Ref. [16] were made using a bottom-mounted, upward-facing acoustic Doppler current profiler (ADCP) in a 15-meter deep water column off the southern New Jersey coast undergoing strong wind and wave forcing. Mean wind stress was 0.1 N/m^2 and mean wave height was 1 m. The

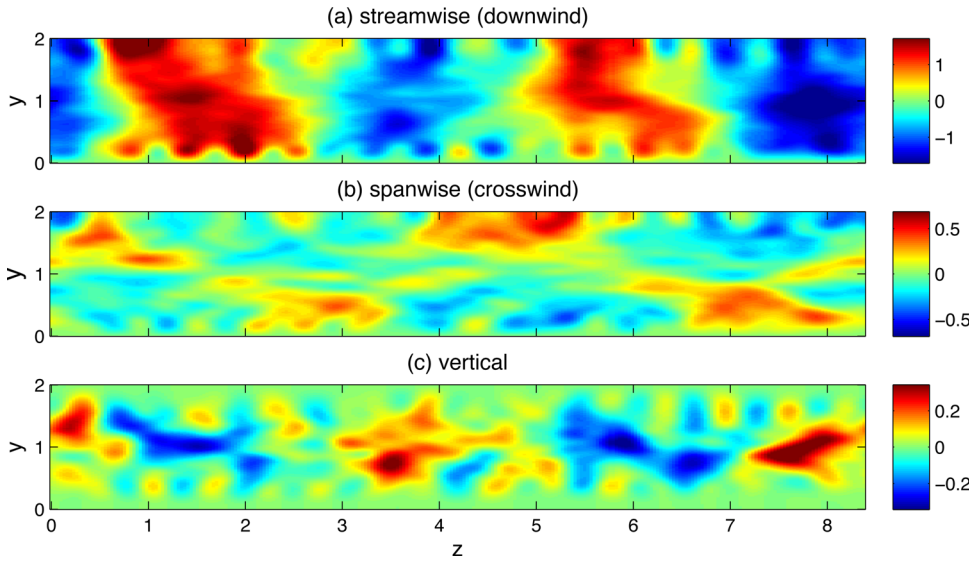

Fig. 6 Crosswind-vertical variation of partially averaged velocity fluctuations v_i' (defined in Eq. (26)) in flow without LC. Results are from the simulation on the 48 × 50 × 48 quadratic NURBS mesh.

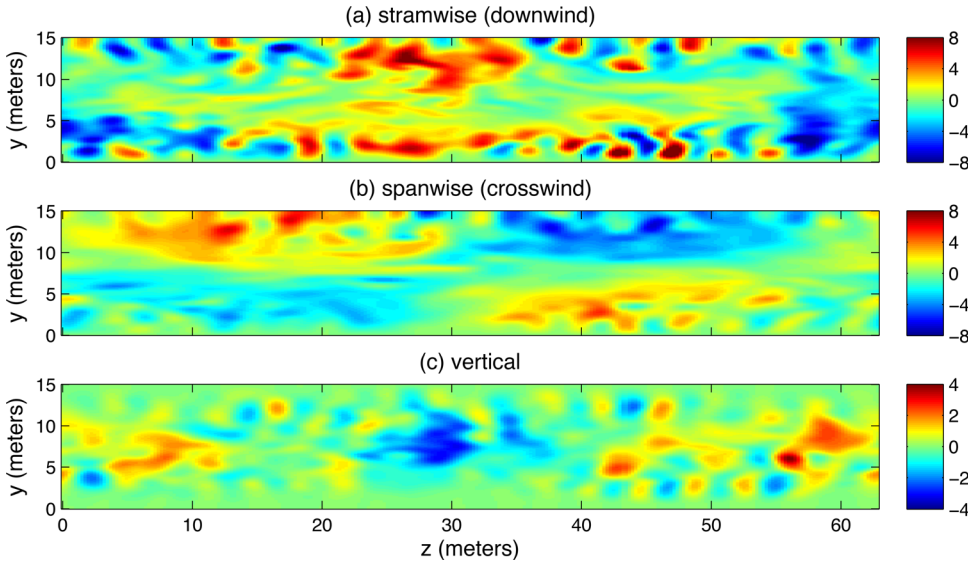

Fig. 7 Crosswind-vertical variation of velocity instantaneous velocity fluctuations u_i' (in cm/s). Results are from the simulation on the $48 \times 50 \times 48$ quadratic NURBS mesh. Computational velocities have been made dimensional with wind stress friction velocity recorded in the field during episodes of full-depth LC [6]. Field measurements were made in a 15-meters deep water column under a wind stress of 0.1 N/m^2.

ADCP was not able to make a reliable measurement of the uppermost 15% of the water column. Furthermore, the computations do not take into account the effect of wave breaking at the surface. Thus comparison between field measurements and the LES should not include the near-surface region. Comparison of panels (*b*) in Figs. 7 and 8 shows that the LES is able to resolve the near-bottom intensification of the full-depth region of positive downwind velocity fluctuations measured in the field. Furthermore, in Fig. 8 note that the region of downwelling (panel (*c*)) coincides with a region of positive downwind velocity fluctuations (panel a), which as described earlier is also the case in the LES (see Figs. 5 and 7).

In conclusion, predictions from our computation with C-L vortex forcing compare favorably with field measurements in Ref. [16] in spite of the low Reynolds number of the computation ($Re = 395$) compared to the Reynolds number of the observations ($Re \approx 50{,}000$).

4.2 Mesh Convergence. Next we present mesh convergence studies on quadratic NURBS meshes in terms of mean downwind velocity and turbulent kinetic energy (TKE) for flow with full-depth LC. Mean velocity, TKE, budgets of TKE and budgets of TKE components for this flow and the corresponding flow without LC have been analyzed in detail in Ref. [9]. Here we focus strictly on mesh convergence. Details of the meshes considered are given in Table 1. Note that for the coarsest mesh of $24 \times 26 \times 24$ elements, the first wall-normal mesh knot is at a distance $y_1^+ = u_\tau \Delta y/\nu = 4.62$. For the the finest mesh of $64 \times 66 \times 64$ elements,

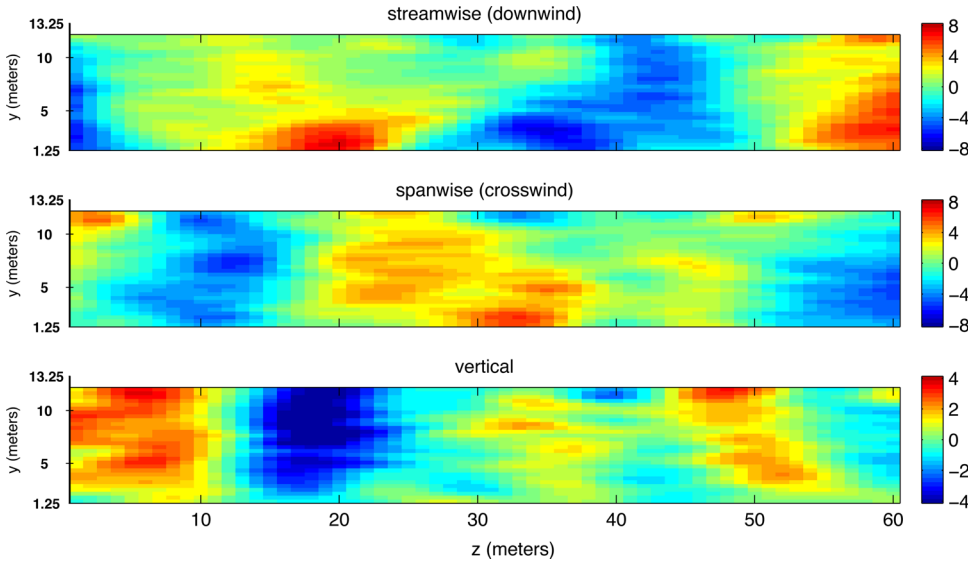

Fig. 8 Crosswind-vertical variation of velocity instantaneous velocity fluctuations u_i' (in cm/s) during episode of full-depth Langmuir cells measured during field experiments of Gargett and Wells [6] using a bottom-mounted, upward-facing acoustic Doppler current profiler (ADCP). Field measurements were made in a 15 ms-deep water column under a wind stress of 0.1 N/m^2. This figure is courtesy of Ann Gargett.

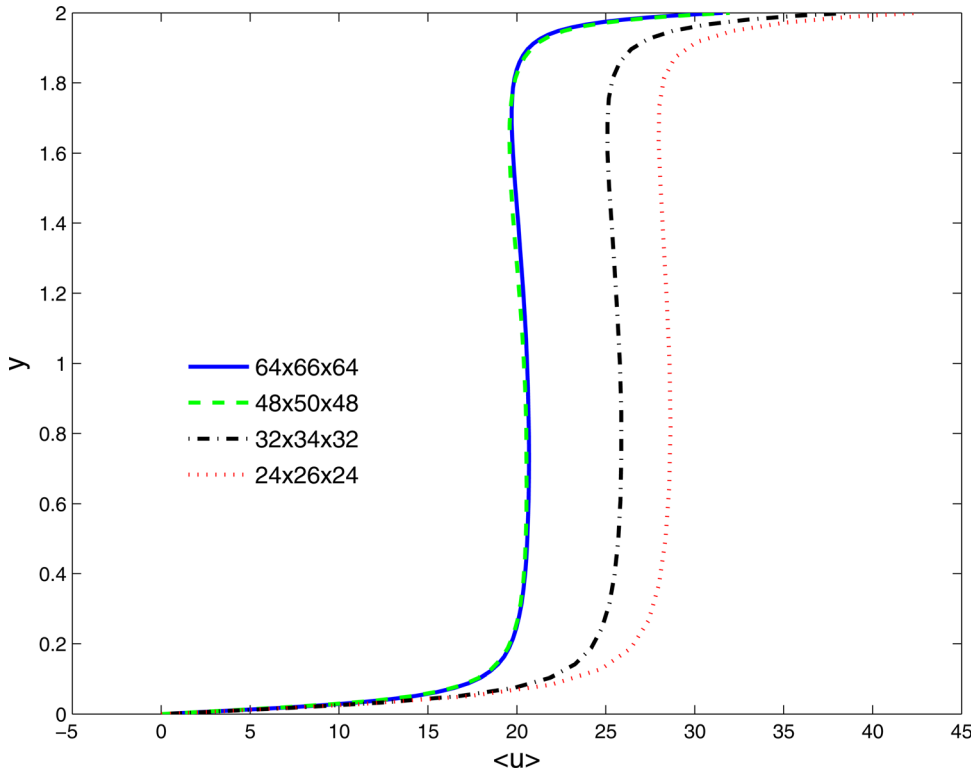

Fig. 9 Convergence of mean downwind velocity in flow with LC. Quadratic NURBS meshes were used for all cases.

$y_1^+ = 1.55$. Thus for all meshes considered, the first point off the bottom (top) is within the viscous sublayer.

Mean downwind velocity is expressed as $\langle u \rangle$, recalling that brackets denote averaging over time and downwind and cross-wind directions. TKE is defined in terms of velocity fluctuations as $\text{TKE} = \langle u'u' + v'v' + w'w' \rangle / 2$, where velocity fluctuations are again obtained via the classical Reynolds decomposition: $\boldsymbol{u} = \langle \boldsymbol{u} \rangle + \boldsymbol{u}'$.

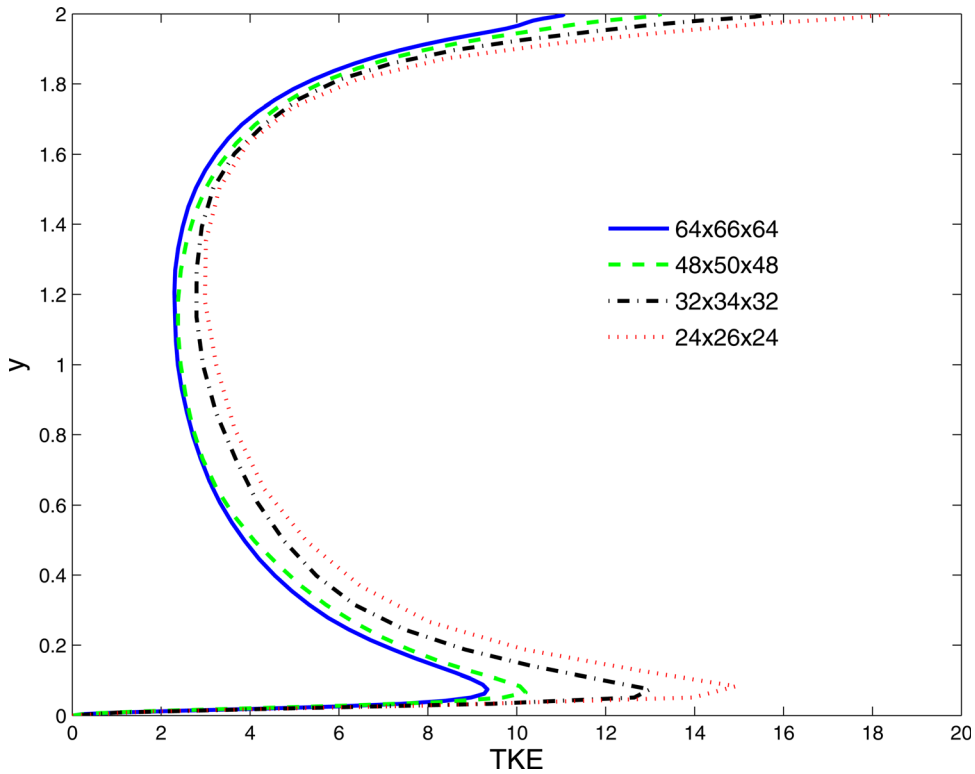

Fig. 10 Convergence of turbulent kinetic energy (TKE) in flow with LC. Quadratic NURBS meshes were used for all cases.

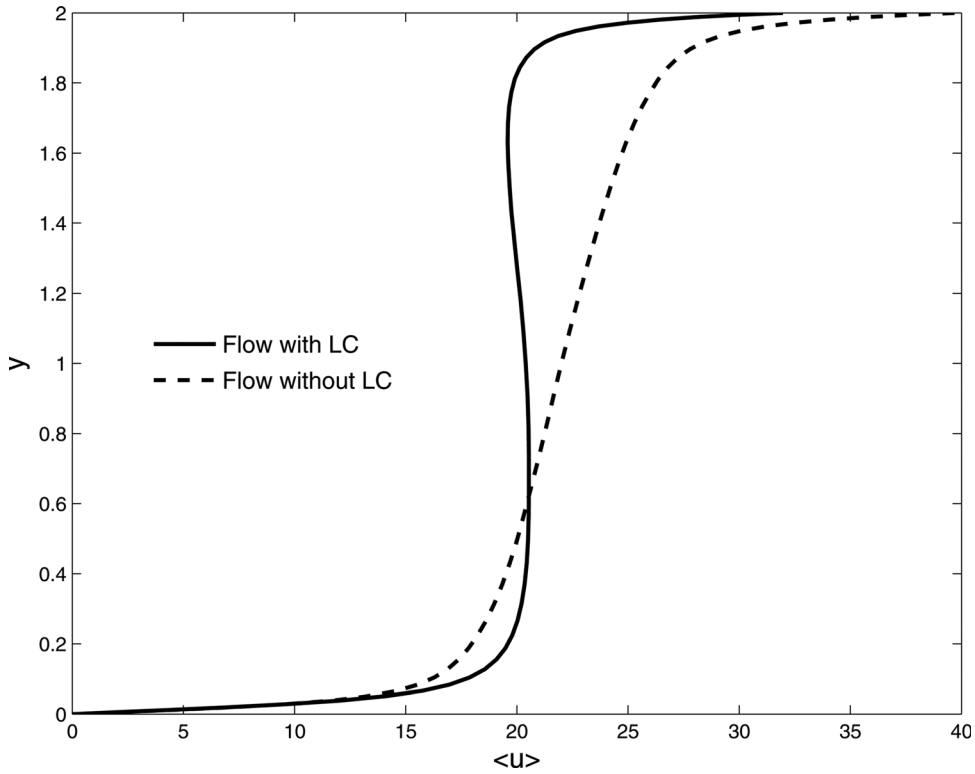

Fig. 11 Mean downwind velocity in flows with and without LC. The $48 \times 50 \times 48$ quadratic NURBS mesh was used for both flows.

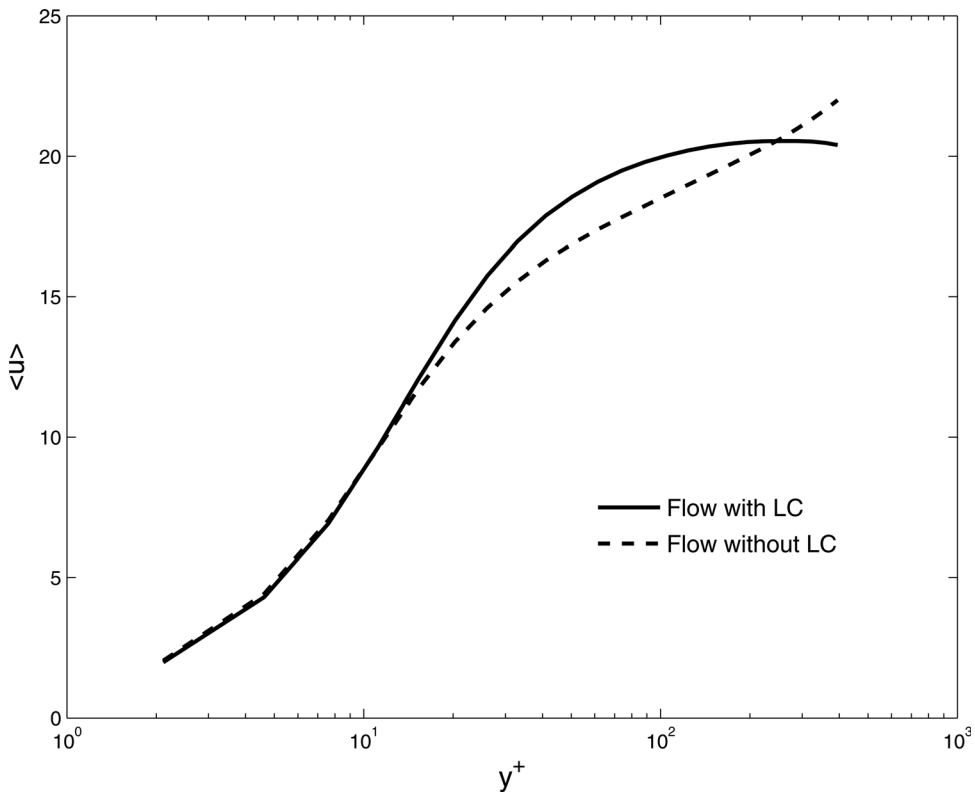

Fig. 12 Mean downwind velocity versus wall-normal (vertical) direction in wall (plus) units in flows with and without LC. The $48 \times 50 \times 48$ quadratic NURBS mesh was used for both flows. Note that $y^+ = u_\tau y/\nu$.

We only present our computational results, because no direct numerical simulation (DNS) of this test case exists that we could use as a benchmark solution. Figure 9 shows convergence of the mean velocity profile. The $24 \times 26 \times 24$ mesh gives a significant over-prediction of the mean flow. The results improve for the $32 \times 34 \times 32$ mesh. Further improvement is seen for the $48 \times 50 \times 48$ mesh. The $64 \times 66 \times 64$ mesh yields a nearly indistinguishable mean velocity profile from the $48 \times 50 \times 48$ case. Similar convergence pattern is observed for the TKE in Fig. 10, however, very small differences between the $48 \times 50 \times 48$ and the $64 \times 66 \times 64$ cases are visible in the figure.

4.3 Disruption of the Log Layer. Figures 11 and 12 provide a comparison between the flow with LC and the same flow without LC in terms of mean velocity in order to highlight the effects induced by LC. The action of LC serves to homogenize momentum throughout the water column leading to a near constant velocity profile in the core region and thinner viscous sublayers at the surface and bottom. Figure 12 shows mean velocity versus wall-normal direction in wall units in the lower half of the water column. The flow without LC exhibits a well-developed, near-bottom log-layer. Meanwhile in the flow with LC, enhanced mixing associated with the Langmuir cells disrupts the classical log-layer region inducing an extended wake region at depths normally characterized by the log-law. A similiar log-layer disruption has been reported in Ref. [21] in their LES of full-depth LC. Disruption of the log-layer by the action of LC has important implications for general coastal ocean circulation models (GCOCMs). Traditional Reynolds Navier-Stokes (RANS) parameterizations of the turbulent bottom boundary layer in GCOCMs assume the presence of a well-developed log-layer. Thus, these parameterizations are not able to properly account for log-layer disruption caused by full-depth LC and ultimately wave-current interaction.

5 Conclusions and Future Work

We have successfully extended variational multiscale turbulence modeling procedures to the C-L equations using isogeometric analysis based on quadratic NURBS. The C-L equations were expressed in semilinear form revealing an advection-diffusion system characterized by nonsymmetric advective matrices. The weak form of this system was treated with the residual-based multiscale formulation in Ref. [20] together with stabilization parameters defined in terms of the aforementioned advective matrices based on the theory presented in Ref. [29]. No-slip conditions were enforced weakly following the approach described in Refs. [23,35,36].

The methodology showed good convergence properties for a wind-driven shear flow characterized by large-scale stream-wise structures (full-depth Langmuir circulation) in agreement with the spectral results in Ref. [9] and the field measurements in Refs. [15,16]. A major impact of the full-depth Langmuir cells was shown to be enhanced mixing of momentum leading to a disruption of the classical near-bottom log-layer.

Future research will use the method developed in this manuscript to investigate effects of complex topography on Langmuir circulation and other mixing processes in coastal oceans and estuaries. Furthermore, we will explore weak enforcement of Dirichlet boundary conditions potentially serving as a model of prohibitively expensive viscous sublayers in continental shelf flows.

Acknowledgment

This research has been supported in part by an appointment to the Postgraduate Research Participation Program at the U.S. Army Engineering Research and Development Center, Coastal and Hydraulics Laboratory (ERDC-CHL) administered by the Oak Ridge Institute for Science and Education through an interagency agreement between the U.S. Department of Energy and ERDC. This research has also been partially supported through NSF Award No. CBET-0846510 and ARO Award No. W911NF-11-1-0083.

References

[1] Donelan, M. A., 1998, "Air-Water Exchange Processes," *Physical Processes in Lakes and Oceans*, J. Imberger, ed., Coastal and Estuarine Studies, American Geophysical Union, pp. 19–36.
[2] Langmuir, I., 1938, "Surface Motion of Water Induced by Wind," Science, **87**, pp. 119–123.
[3] Thorpe, S. A., 2004, "Langmuir Circulation," Annu. Rev. Fluids Mech., **36**, pp. 55–79.
[4] Craik, A. D. D., and Leibovich, S., 1976, "A Rational Model for Langmuir Circulation," J. Fluid Mech., **73**, pp. 401–426.
[5] McWilliams, J. C., Sullivan, P., and Moeng, C.-H., 1997, "Langmuir Turbulence in the Ocean," J. Fluid Mech., **334**, pp. 31–58.
[6] Sullivan, P. P., and McWilliams, J. C., 2010, "Dynamics of Winds and Currents Coupled to Surface Waves," Annu. Rev. Fluids Mech., **42**, pp. 19–42.
[7] Kantha, L., Lass, H. U., and Prandke, H., 2010, "A Note on Stokes Production of Turbulence Kinetic Energy in the Oceanic Mixed Layer: Observations in the Baltic Sea," Ocean Dyn., **60**, pp. 171–180.
[8] Sullivan, P. P., McWilliams, J. C., and Melville, W. K., 2007, "Surface Gravity Wave Effects in the Oceanic Boundary Layer: Large-Eddy Simulaion with Vortex Force and Stochastic Forcing," J. Fluids Mech., **593**, pp. 405–452.
[9] Tejada-Martínez, A. E., and Grosch, C. E., 2007, "Langmuir Turbulence in Shallow Water. Part 2. Large-Eddy Simulation," J. Fluid Mech., **576**, pp. 63–108.
[10] Skyllingstad, E. D., and Denbo, D. W., 1995, "A Ocean Large-Eddy Simulation of Langmuir Circulations and Convection in the Surface Mixed Layer," J. Geophys. Res., **100**, pp. 501–522.
[11] Li, M., Garrett, C., and Skyllingstad, E., 2005, "A Regime Diagram for Classifying Turbulent Large Eddies in the Upper Ocean," Deep-Sea Res., **52**, pp. 259–278.
[12] D'Alessio, S. J., Abdella, K., and McFarlane, N. A., 1998, "A New Second-Order Turbulence Closure Scheme for Modeling the Oceanic Mixed Layer," J. Phys. Oceanogr., **28**, pp. 1624–1641.
[13] Kantha, L., and Clayson, C. A., 2004, "On the Effect of Surface Gravity Waves on Mixing in the Oceanic Mixed Layer," Ocean Modelling, **6**, pp. 101–124.
[14] Pope, S. B., 2000, *Turbulent Flows*, Cambridge University Press, Cambridge.
[15] Gargett, A. E.,Wells, J. R., Tejada-Martínez, A. E., and Grosch, C. E., 2004, "Langmuir Supercells: A Mechanism for Sediment Resuspension and Transport in Shallow Seas," Science, **306**, pp. 1925–1928.
[16] Gargett, A. E., and Wells, J. R., 2007, "Langmuir Turbulence in Shallow Water. Part 1. Observations," J. Fluids Mech., **576**, pp. 27–61.
[17] Polton, J. A., Smith, J. A., MacKinnon, J. A., and Tejada-Martínez, A. E., 2008, "Rapid Generation of High-Frequency Internal Waves Beneath a Wind and Wave Forced Oceanic Mixed Layer," Geophys. Res. Lett., **35**, p. L14602.
[18] Kukulka, T., Plueddeman, A., Trowbridge, J., and Sullivan, P. P., 2009, "Significance of Langmuir Circulation in Upper Ocean Mixing: Comparison of Observations and Simulations," Geophys. Res. Lett., **36**, p. L10603.
[19] Hughes, T., Cottrell, J., and Bazilevs, Y., 2005, "Isogeometric Analysis: CAD, Finite Elements,NURBS, Exact Geometry, and Mesh Refinement," Comput. Methods Appl. Mech. Eng., **194**, pp. 4135–4195.
[20] Bazilevs, Y., Calo, V., Cottrel, J., Hughes, T., Reali, A., and Scovazzi, G., 2007, "Variational Multiscale Residual-Based Turbulence Modeling for Large Eddy Simulation of Incompressible Flows," Comput. Methods Appl. Mech. Eng., **197**, pp. 173–201.
[21] Tejada-Martínez, A. E., Grosch, C. E., Gargett, A. E., Polton, J. A., Smith, J. A., and MacKinnon, J. A., 2009, "A Hybrid Spectral/Finite-Difference Large-Eddy Simulator of Processes in the Upper Ocean," Ocean Modelling, **39**, pp. 115–142.
[22] Akkerman, I., Bazilevs, Y., Calo, V., Hughes, T., and Hulshoff, S., 2008, "The Role of Continuity in Residual-Based Variational Multiscale Modeling of Turbulence," Comput. Mech., **41**, pp. 371–378.
[23] Bazilevs, Y., and Hughes, T., 2007, "Weak Imposition of Dirichlet Boundary Conditions in Fluid Mechanics," Computers and Fluids, **36**, pp. 12–26.
[24] Brooks, A. and Hughes, T., 1982, "Streamline Upwind/Petrov-Galerkin Formulations for Convection Dominated Flows with Particular Emphasis on the Incompressible Navier-Stokes Equations," Comput. Methods Appl. Mech. Eng., **32**, pp. 199–259.
[25] Tezduyar, T., 2003, "Computation of Moving Boundaries and Interfaces and Stabilization Parameters," Int. J. Numer. Methods Fluids, **43**, pp. 555–575.
[26] Hughes, T., Scovazzi, G., and Franca, L., 2004, "Multiscale and Stabilized Methods," *Encyclopedia of Computational Mechanics, Vol. 3, Computational Fluid Dynamics*, E. Stein, R. de Borst, and T. J. R. Hughes, eds., Wiley, New York, Chap. 2.
[27] Hughes, T., and Mallet, M., 1986, "A New Finite Element Formulation for Fluid Dynamics: III. The Generalized Streamline Operator for Multidimensional Advective-Diffusive Systems," Comput. Methods Appl. Mech. Eng., **58**, pp. 305–328.
[28] Hughes, T., Franca, L., and Mallet, M., 1987, "A New Finite Element Formulation for Fluid Dynamics: VI. Convergence Analysis of the Generalized SUPG Formulation for Linear Time-Dependent Multidimensional Advective-Diffusive Systems," Comput. Methods Appl. Mech. Eng., **63**, pp. 97–112.
[29] Shakib, F., Hughes, T., and Johan, Z., 1991, "A New Finite Element Formulation for Computational Fluid Dynamics: X. The Compressible Euler and

Navier-Stokes Equations," Comput. Methods Appl. Mech. Eng., **89**, pp. 141–219.
[30] Johnson, C., 1987, *Numerical Solution of Partial Differential Equations by the Finite Element Method*, Cambridge University Press, London.
[31] Denman, E., and Beavers, A., 1976, "The Matrix Sign Function and Computations in Systems," Appl. Math. Comput., **2**, pp. 63–94.
[32] Bazilevs, Y., and Akkerman, I., 2010, "Large Eddy Simulation of Turbulent Taylor-Couette Flow Using Isogeometric Analysis and the Residual-Based Variational Multiscale Method," J. Comp. Phys. **229**(9), pp. 3402–3414.
[33] Tezduyar, T., and Osawa, Y., 2000, "Finite Element Stabilization Parameters Computed from Element Matrices and Vectors," Comput. Methods Appl. Mech. Eng., **190**, pp. 411–430.
[34] Hsu, M., Bazilevs, Y., Calo, V., Tezduyar, T., and Hughes, T., 2010, "Improving Stability of Multiscale Formulations of Fluid Flow at Small Time Steps," Comput. Methods Appl. Mech. Eng., **199**, pp. 828–8240.
[35] Bazilevs, Y., Michler, C., Calo, V., and Hughes, T., 2007, "Weak Dirichlet Boundary Conditions for Wall-Bounded Turbulent Flows," Comput. Methods Appl. Mech. Eng., **196**, pp. 4853–4862.
[36] Bazilevs, Y., Michler, C., Calo, V., and Hughes, T., 2010, "Isogeometric Variational Multiscale Modeling of Wall-Bounded Turbulent Flows with Weakly-Enforced Boundary Conditions on Unstretched Meshes," Comput. Methods Appl. Mech. Eng., **199**, pp. 780–790.
[37] Phillips, O. M., 1966, *The Dynamics of the Upper Ocean*, Cambridge University Press, Cambridge.
[38] LeBlond, P. H., and Mysak, L. A., 1977, *Waves in the Ocean*, Elsevier, New York.
[39] Harcourt, R. R., and D'Asaro, E. A., 2008, "Large Eddy Simulation of Langmuir Turbulene in Pure Wind Seas," J. Phys. Oceanogr., **38**, pp. 1542–1562.
[40] Chung, J., and Hulbert, G. M., 1993, "A Time Integration Algorithm for Structural Dynamics with Improved Numerical Dissipation: The Generalized-α method," J. Appl. Mech., **60**, pp. 371–75.
[41] Jansen, K. E., Whiting, C. H., and Hulbert, G. M., 1999, "A Generalized-α Method for Integrating the Filtered Navier-Stokes Equations with a Stabilized Finite Element Method," Comput. Methods Appl. Mech. Eng., **190**, pp. 305–319.